

Intrinsic Charge Transport in Stanene: Roles of Bucklings and Electron-Phonon Couplings

Yuma Nakamura¹, Tianqi Zhao¹, Jinyang Xi, Wen Shi, Dong Wang, and Zhigang Shuai**

¹These authors contributed equally

Y. Nakamura, T. Zhao, W. Shi, Prof. D. Wang, Prof. Z. Shuai

MOE Key Laboratory of Organic OptoElectronics and Molecular Engineering, Department of Chemistry, Tsinghua University, Beijing 100084, P. R. China

E-mail: dong913@tsinghua.edu.cn, zgshuai@tsinghua.edu.cn

Dr. J. Xi

Materials Genome Institute, Shanghai University, Shanghai 200444, P. R. China

Prof. Z. Shuai

Key Laboratory of Organic Solids, Beijing National Laboratory for Molecular Science (BNLMS), Institute of Chemistry, Chinese Academy of Science, Beijing 100190, P. R. China

Prof. Z. Shuai

Collaborative Innovation Center of Chemistry for Energy Materials, Xiamen University, Xiamen 351005, P. R. China

Y. Nakamura

Institute for Materials Research, Tohoku University, Sendai 980-8577, Japan

Abstract

The intrinsic charge transport of stanene is investigated by using density function theory and density function perturbation theory coupled with Boltzmann transport equations from first principles. The accurate Wannier interpolations are applied to calculate the charge carrier scatterings with all branches of phonons with dispersion contribution from full first Brillouin zone wave-vectors. The intrinsic electron and hole mobilities are predicted to be $2\sim3\times10^3\text{ cm}^2\text{ V}^{-1}\text{ s}^{-1}$ at 300 K, and we find that the intervalley scatterings from the out-of-plane and transverse acoustic modes of phonons dominate the carrier relaxation determining the carrier transport. In contrast, the intrinsic carrier mobilities obtained by the conventional deformation potential approach (Long et al., J. Am. Chem. Soc. 2009, 131, 17728) are found to be as large as $2\sim3\times10^6\text{ cm}^2\text{ V}^{-1}\text{ s}^{-1}$ at 300 K, in which the longitudinal acoustic phonons are assumed to be the only scattering mechanism. The inadequacy of the deformation potential approximation in stanene is attributed to the buckling of the honeycomb structure, which originates from the $\text{sp}^2\text{-sp}^3$ orbital hybridization and results in broken planar symmetry as compared to graphene. The high carrier mobility of stanene renders it a promising candidate in nanoelectronics and spintronics applications and we propose to enhance its carrier mobilities by suppressing the out-of-plane vibrations by substrate suspension or clamping.

Keywords: stanene, electron-phonon couplings, carrier mobility calculation, density functional perturbation theory, two-dimensional materials

1. Introduction

Motivated by the peculiar behavior of electronic structure with Dirac cone in graphene,^[1–4] the class of two-dimensional (2D) materials have received intensive interests in recent years.^[5] The group-IV elemental analogues of graphene, including silicene,^[6] germanene,^[7] and stanene,^[8–11] are promising alternatives going beyond graphene owing to their outstanding electronic properties. The experimental realizations by molecular beam epitaxy further promote the promising applications.^[6,7,11] Among these group IV elemental 2D sheets, stanene draws particular attention since the theory predicted that it can be a large-gap topological insulator,^[12–15] which promises applications in dissipationless electronics. Moreover, stanene could also show versatility for enhanced thermoelectric performance,^[16,17] near-room-temperature quantum anomalous effect^[18] and topological superconductivity.^[19,20] For these applications, carrier transport lies in the center of electronic processes. The electron-phonon (el-ph) scatterings play an essential role in determining the intrinsic transport properties. For evaluating the intrinsic carrier mobility for 2D materials, Long *et al.*^[21,22] have first applied the deformation potential approximation (DPA) of Shockley and Bardeen,^[23] which only takes into account the scattering by longitudinal acoustic (LA) phonons. Such approach is conceptually simple but has been extremely successful as has been widely applied in calculating the intrinsic carrier mobility of 2D sheets or nanoribbons, such as graphene,^[24–28] graphdiyne,^[22,24] phosphorene,^[29] silicene,^[30] transition metal dichalcogenide,^[31] as well as perovskites.^[32]

DPA can overestimate the intrinsic room temperature mobility since it considers only longitudinal acoustic phonon scattering process. In the case of silicene, DPA presented a mobility value of $2 \times 10^5 \text{ cm}^2 \text{ V}^{-1} \text{ s}^{-1}$.^[30] But when using density functional perturbation theory (DFPT) which account for electron scatterings with all branches of phonons for silicene, the mobility was reduced to be $2.1 \times 10^3 \text{ cm}^2 \text{ V}^{-1} \text{ s}^{-1}$.^[33] Indeed, the reduced symmetry of stanene (D_3) compared to graphene (D_6) may cause additional scattering processes with phonons other

than LA.^[34] The room temperature mobility of iodine-functionalized stanene nanoribbons have been studied by using Kubo-Greenwood formalism, in which el-ph couplings are evaluated by calculating deformation potentials for longitudinal and transverse acoustic phonons.^[35]

In this work, we provide a detailed characterization of the role of different acoustic and optical phonons scatterings in the carrier transport of stanene. The state-of-the-art density functional theory (DFT), density functional perturbation theory (DFPT)^[36] and Wannier interpolation scheme^[37] as implemented in the Quantum ESPRESSO,^[38] Wannier90,^[39] and EPW packages^[40,41] were employed to obtain the ultra-dense electronic band structures, phonon dispersion and el-ph coupling matrix elements. With all these ingredients, the Boltzmann transport theory with relaxation time approximation was used to determine the charge carrier mobilities. Buckling in the hexagonal honeycomb structure of stanene, originating from the sp²-sp³ orbital hybridization^[42-44] can make big difference from the the planar structures such as graphene or graphynes, where huge intrinsic mobility $\sim 10^5 \text{ cm}^2 \text{ V}^{-1} \text{ s}^{-1}$ has been predicted.^[22] We note that the mobility in buckling structured monolayer MoS₂ was found to be $\sim 410 \text{ cm}^2 \text{ V}^{-1} \text{ s}^{-1}$ ^[31,45,46] and phosphorene to be $\sim 170 \text{ cm}^2 \text{ V}^{-1} \text{ s}^{-1}$.^[29] It is thus intriguing to investigate the roles of el-ph couplings for all phonon modes in the buckled stanene sheet.

2. Results and Discussion

2.1. Electronic structures and phonon band dispersions

The crystal structures of stanene are illustrated in **Figure 1(a)**. The optimized lattice constant is 4.676 Å, which is in good agreement with previous calculations (4.676 Å^[9] or 4.673 Å^[10]) under the generalized-gradient approximation (GGA). In experiment, the lattice constant of stanene matches with that of Bi₂Te₃ substrate (4.383 Å).^[11] The obtained buckling width 0.85 Å is in good agreement with previous theoretical works.^[10] The buckling of

stanene may depend on chemical environment and the experimental buckling value of stanene on Bi_2Te_3 substrate was found to be 1.2 ± 0.2 Å: it is known that the strain may enhance the magnitude of buckling of stanene from 0.85 to 1.09 Å.^[11] The unit cell of stanene consists of two sublattices and the reciprocal space is shown in Figure 1(b) with the first Brillouin zone (BZ) and high symmetry points Γ , \mathbf{K} , \mathbf{K}' and \mathbf{M} . The Dirac cones, or valley is seen in \mathbf{K} and \mathbf{K}' (Dirac points), which are inequivalent to each other. The band structures of stanene are depicted in Figure 1(c) to compare with that of graphene. Similar to graphene, the Dirac cones of stanene appear at \mathbf{K} and \mathbf{K}' in the first BZ if spin orbital coupling is ignored. However, a bandgap 76 meV is opened when spin-orbital coupling (SOC) was considered for stanene (Figure 1(c)), which is consistent with previous work of 73 meV.^[10] This bandgap opening indicates the possibility to realize topological insulator phase. We obtain the Fermi velocities of 1.44×10^6 m s⁻¹ and 0.83×10^6 m s⁻¹ at the Dirac point for graphene and stanene, respectively. The smaller the Fermi velocity in stanene is caused by the less dispersive band structure near the Dirac point.

For the sake of reducing the computation load, SOC is not considered in the phonon and el-ph coupling calculations. The phonon dispersion relations of stanene and graphene are shown in Figure 1(d). For group IV elemental 2D sheets, phonon branches are classified as out-of-plane acoustic (ZA), transverse acoustic (TA), longitudinal acoustic (LA), out-of-plane optical (ZO), transverse optical (TO), and longitudinal optical (LO). TA and LA modes show linear dispersion near Γ point. However, the flexural ZA mode obeys a quadratic dispersion $\omega_{ZA} \propto |\mathbf{q}|^2$, which is attributed to threefold rotational symmetry in stanene and sixfold rotational symmetry in graphene.^[42,47,48] The obtained phonon frequency of stanene is about 10 times smaller than that of graphene because of the much heavier atomic mass in stanene. The crossing between LA and ZO occurred in graphene is absent in stanene.

2.2. Full electron phonon coupling and deformation potential approximation

In order to elucidate the role of different phonon modes on charge carrier scattering, we depict the square of the el-ph coupling matrix elements (see Equation (3) in methodological part) for the Dirac point \mathbf{K} in the conduction band of stanene and graphene as a function of phonon wavevector \mathbf{q} over the full first BZ (Figure 2). The phonon wavevector are depicted in fractional coordinates, with Γ (0, 0, 0), \mathbf{K} (1/3, 1/3, 0) and \mathbf{K}' (2/3, 2/3, 0). Regions satisfying the momentum conservation law $\mathbf{k}' = \mathbf{k} + \mathbf{q}$ may contribute to carrier scattering. Around the BZ center ($\mathbf{q} = \Gamma$), the el-ph coupling demonstrates intravalley transition, while for phonon wave vectors near the edge of BZ (for example $\mathbf{q} = \mathbf{K}$, \mathbf{K}') they demonstrate intravalley transition. For the TA and LA modes in stanene, we observed that the intensity of el-ph coupling over the intervalley scattering regions are complementary, that is, the regions with large (small) scattering with TA are always with small (large) scattering with LA. The TA mode shows high intensity in the intervalley region, whereas LA mode does not.^[28,33] This complementary behavior between TA and LA has been demonstrated in silicene.^[33] The geometrical pattern of el-ph coupling matrix for stanene is more complicated for the coupling matrix over the full first BZ, which may be ascribed to broken horizontal mirror symmetry. It is also found that the el-ph coupling strength for stanene is about one tenth of those in graphene for all modes of vibrations. This indicates that the vibrations have weaker effect on electrons in stanene, which agree with the trend from graphene to silicene.^[33]

Near the center of BZ, the el-ph coupling matrix for LA is linear with $|\mathbf{q}|$ (see Equation (12) in methodology part). The slope gives rise to the deformation potential for LA, denoted as D_{LA} . This quantity can also be obtained by dilating the unit cell and measuring the change of Fermi level with respect to strains (SI Figure S2).^[21,22] Table 1 shows that the two methods can give consistent results. The D_{LA} for graphene along zigzag and armchair direction are almost the same (5.14 eV and 5.0 eV), which are also in agreement with previous theoretical results.^[21,24,27,30] Stanene also shows almost the same D_{LA} along zigzag and armchair

directions, but its value is one order of magnitude smaller D_{LA} compared to graphene. Since D_{LA} manifests the electron coupling strength with LA, this is in consistent with the above result that the el-ph coupling strength for stanene is one-order-of magnitude weaker than graphene. It is also consistently observed that D_{LA} decreases from graphene (5.0 eV) to silicene (2.13),^[30] germanene (1.16),^[30] and stanene (0.48). This trend has been attributed to the increasing bulking, which is 0.0 Å, 0.45 Å, 0.69 Å, 0.85 Å, for graphene, silicene, germanene, and stanene, respectively.^[8,10,44,49] The elastic constants also show decreasing trend from graphene (328.30 J m⁻¹) to silicene (85.99 J m⁻¹),^[30] germanene (55.98 J m⁻¹),^[30] and stanene (28.5 J m⁻¹). According to the deformation theory, the mobility $\mu \propto C_{ii}/D_{LA}^2$. The decrease trend of D_{LA} leads an increasing trend of mobility μ . However, the reduced symmetry of stanene (D_3) compared to graphene (D_6) may cause additional scattering processes with phonons other than LA.^[42,47,48] We account for the scattering from other modes of vibrations in the following.

2.3. Intrinsic carrier mobility

According to Boltzmann transport theory, the carrier mobility can be expressed in Equation (1) where the electron group velocity (determined by band structure) and the relaxation time are needed. The latter is the inverse of the el-ph scattering rate expressed by Equation (2) in the methodology part where the knowledge of electronic structure, phonon dispersion and el-ph coupling matrix elements are needed in both \mathbf{k} and \mathbf{q} spaces.

The calculated scattering rates at the Dirac point for both stanene and graphene are shown in Table 2. It is found that for graphene, the main contribution of scatterings is from the LA mode, whereas the scatterings with ZA mode are negligible due to the mirror symmetry. However, for stanene, the scatterings with ZA and TA mode are significantly larger than LA mode. In the deformation theory, LA mode is the only scattering mechanism,

which holds in graphene, but not in stanene. Indeed, the room temperature mobility of graphene derived from deformation potential theory is in agreement with that calculated by evaluating the el-ph coupling for all phonon modes (Table S1).^[25]

We demonstrate the phonon branch-resolved scattering relaxation time as a function of temperature in Figure 3, again for stanene and graphene for the sake of comparison. As expected, for graphene, the curve of “Total” fully coincides with “LA”. But for stanene, “LA” curve is far from the “Total”. Instead, “ZA” and “TA” curves are closer to the “Total”, even the “LO” contribution being not negligible. Thus, it is not surprising to find that the room temperature mobility of stanene derived from deformation potential theory is three orders of magnitude larger than that calculated by evaluating the el-ph coupling for all phonon modes (Table S1). The resolved the scattering rates from the three acoustic phonon branches (TA, ZA, LA) into intervalley and intravalley scattering contributions are listed in Table 3. For the LA mode, the intravalley scattering dominates intervalley for both graphene and stanene. However, the situation is reversed for TA and ZA modes in stanene, where intervalley scatterings overwhelm the intravalley scatterings. In graphene, intervalley scattering is minor contribution for all three acoustic phonon modes. We notice that the large intervalley scattering is also reported for silicene.^[33] Therefore, the intervalley TA and ZA for stanene play a dominant role in carrier scattering and the inadequacy of DPA in stanene can be attributed to the overlook of TA and ZA modes.

The variation of the phonon-limited mobility of stanene with temperature is shown in **Figure 4**. The acoustic phonon modes dominate the optical phonon modes over the whole temperature range. The out-of-plane and transverse acoustic phonon modes dominate longitudinal acoustic phonon in stanene. The total mobility obeys a power lower of $\mu \propto T^{-\gamma}$, where $\gamma = 1.43$. The intrinsic room-temperature mobility of stanene $2 \sim 3 \times 10^3 \text{ cm}^2 \text{ V}^{-1} \text{ s}^{-1}$ is two order of magnitude lower than that of graphene ($2 \times 10^5 \text{ cm}^2 \text{ V}^{-1} \text{ s}^{-1}$).^[21,24,25] Although the

weaker el-ph couplings in stanene favor high carrier mobility, mobility of stanene is smaller. This is not obscure since the phonon frequency of stanene is one order of magnitude lower than that of graphene. The largest frequency of stanene is smaller than 25 meV, this means that all the phonon modes are excited at room temperature. Besides, the smaller slopes of band structures provide more scattering space in stanene, which further increasing the scattering rates.

3. Conclusion

To summarize, the phonon-limited charge carrier transport properties of stanene have been studied by performing first-principles DFPT calculations with Wannier interpolation. The intrinsic room-temperature (300 K) mobility of $2\sim3\times10^3$ cm^2 V^{-1} s^{-1} is found to be dominated by the intervalley scattering process of the out-of-plane acoustic (ZA) and transverse acoustic (TA) modes. The widely employed deformation potential approximation assumes the dominant role of LA phonons near the center of the BZ and presents the mobility to be $2\sim3\times10^6$ cm^2 V^{-1} s^{-1} , an overestimation by three orders of magnitude, demonstrating the importance of the out-of-plane vibrations in stanene. When the out-of-plane acoustic phonon (ZA) is excluded, which could be realized by substrate suspension or clamping experimentally, the mobility value would be doubled to $5\sim6\times10^3$ cm^2 V^{-1} s^{-1} . We demonstrate the dominant role of the out-of-plane phonon modes for 2D materials, which is an unusual case. The intrinsic mobility of stanene is calculated to be several times larger than those of monolayer MoS₂ and phosphorene. The high carrier mobility of stanene renders it a promising candidate in nanoelectronics and spintronics applications.

4. Methodological approach

Charge carrier mobility and electron-phonon couplings. In the Boltzmann transport theory, the carrier mobility is expressed as^[25]

$$\mu = \frac{\sum_{nk} e v_{nk}^2 \tau_{nk} \left(-\frac{\partial f_{nk}^0}{\partial \epsilon_{nk}} \right)}{\sum_{nk} f_{nk}^0} \quad (1)$$

where ϵ_{nk} , v_{nk} and τ_{nk} are the electron energy, group velocity and relaxation time for the electronic state with band index n and wavevector \mathbf{k} . f_{nk}^0 is the Fermi-Dirac distribution and e is the elementary charge. n is summed over conduction (valence) bands for electrons (holes). The group velocity is expressed as $v_{nk} = \frac{1}{h} \nabla_{\mathbf{k}} \epsilon_{nk}$. The parameter τ_{nk} is of prime importance in describing the scattering mechanism of charge carriers. τ_{nk} can be expressed as^[25]

$$\frac{1}{\tau_{nk}} = \sum_{n',\lambda q} |g_{\lambda q}(\mathbf{k}, n, n')|^2 \left(1 - \cos \theta_{\mathbf{k}, \mathbf{k}+q} \right) \left[\begin{aligned} & \left(f_{n'k+q}^0 + n_{\lambda q}^0 \right) \delta \left(\epsilon_{n'k+q} - \epsilon_{nk} - h\omega_{\lambda q} \right) \\ & + \left(1 + n_{\lambda q}^0 - f_{n'k+q}^0 \right) \delta \left(\epsilon_{n'k+q} - \epsilon_{nk} + h\omega_{\lambda q} \right) \end{aligned} \right] \quad (2)$$

where the sum is take over all the conduction (valence) band n' for electrons (holes) and all modes of phonon with mode index λ and wavevector \mathbf{q} . $\omega_{\lambda q}$ and $n_{\lambda q}^0$ are the frequency and Bose-Einstein distribution of phonons. ϵ_{nk} and $\epsilon_{n'k+q}$ is the electronic energy of the initial state with band index n and wavevector \mathbf{k} and the final state band index n' and wavevector $\mathbf{k} + \mathbf{q}$, $\theta_{\mathbf{k}, \mathbf{k}+q}$ is the scattering angle between the initial and final states. $f_{n'k+q}^0$ is the Fermi-Dirac distribution of the final state. $g_{\lambda q}(\mathbf{k}, n, n')$ is the key parameter of el-ph coupling matrix element. Within the density function perturbation theory, $g_{\lambda q}(\mathbf{k}, n, n')$ is calculated as^[36]

$$g_{\lambda q}(\mathbf{k}, n, n') = \sqrt{\frac{h}{2M\omega_{\lambda q}}} \langle \psi_{n'k+q} | \frac{\partial V_{KS}}{\partial u_{\lambda q}} \cdot \mathbf{e}_{\lambda q} | \psi_{nk} \rangle \quad (3)$$

where $\frac{\partial V_{KS}}{\partial u_{\lambda q}}$ is the first-order derivative of the self-consistent Kohn-Sham potential V_{KS}

with respect to the atomic displacement $u_{\lambda q}$ of phonon mode λ and wavevector \mathbf{q} . $\mathbf{e}_{\lambda q}$

is the phonon polarization vector, $|\psi_{n\mathbf{k}}\rangle$ and $|\psi_{n'\mathbf{k}+\mathbf{q}}\rangle$ are the electronic initial and final Bloch state, respectively.

To calculate relaxation time and mobility from Eqs. (1) and (2), we need to obtain ultra-dense electronic band structure, phonon dispersion, and el-ph coupling matrix elements over a fine grid of \mathbf{k} and \mathbf{q} meshes, which is tremendously computationally laborious at the first principles level. However, by implementing the approximate Wannier-Fourier interpolation scheme, accurate electronic energies, phonon frequencies, and el-ph coupling matrix elements can be obtained with reasonable computational load. Within such a scheme, the electron Hamiltonian H_k^{el} with diagonal elements being the eigenstates of electrons, lattice dynamical matrix D_q^{ph} and el-ph coupling matrix elements $g_{\lambda q}(\mathbf{k}, n, n')$ are firstly calculated on a coarse \mathbf{k} and \mathbf{q} mesh $N_1^{k(q)} \times N_2^{k(q)} \times N_3^{k(q)}$; Secondly, the electronic Hamiltonian are transformed from Bloch space to Wannier space by using a gauge matrix $\{U_k\}$ by

$$H_{\mathbf{R}_e, \mathbf{R}'_e}^{el} = \sum_{\mathbf{k}} e^{-i\mathbf{k}(\mathbf{R}'_e - \mathbf{R}_e)} U_{\mathbf{k}}^\dagger H_{\mathbf{k}}^{el} U_{\mathbf{k}} \quad (4)$$

where the gauge matrix $U_{\mathbf{k}}$ is obtained by the maximally localized Wannier functions (MLWFs) method.^[37,50] \mathbf{R}_e and \mathbf{R}'_e are the lattice vectors in real space, which are also the index of Wannier functions. The lattice dynamical matrix is then Fourier transformed to Wannier space by using the phonon eigenvector matrix $\{\mathbf{e}_q\}$

$$D_{\mathbf{R}_p, \mathbf{R}'_p}^{ph} = \sum_{\mathbf{q}} e^{-i\mathbf{q}(\mathbf{R}'_p - \mathbf{R}_p)} \mathbf{e}_q D_q^{ph} \mathbf{e}_q^\dagger \quad (5)$$

where \mathbf{R}_p and \mathbf{R}'_p are the lattice vectors in real space for phonons. The el-ph coupling matrix is then transformed as ^[51]

$$g(\mathbf{R}_e, \mathbf{R}_p) = \frac{1}{N_p} \sum_{k,q} e^{-i(\mathbf{k} \cdot \mathbf{R}_e + \mathbf{q} \cdot \mathbf{R}_p)} U_{k+q}^\dagger g(\mathbf{k}, \mathbf{q}) U_k e_q^{-1} \quad (6)$$

where $N_p = N_1^q \times N_2^q \times N_3^q$ is the number of unit cells in real space and we have omitted the band and phonon mode index in $g(\mathbf{k}, \mathbf{q})$ for simplicity. Since the quantities $H_{\mathbf{R}_e, \mathbf{R}'_p}^{el}$, $D_{\mathbf{R}_p, \mathbf{R}'_p}^{ph}$, and $g(\mathbf{R}_e, \mathbf{R}_p)$ decay rapidly in Wannier space, we can make truncation in the summation in real space. Finally we can obtain the electronic energy, phonon frequency and electron-phonon coupling matrix elements on a fine \mathbf{k} and \mathbf{q} mesh $N_1'^k(q) \times N_2'^k(q) \times N_3'^k(q)$ by diagonalizing the following matrix

$$H_{\mathbf{k}'}^{el} = U_{\mathbf{k}'} \left(\frac{1}{N_e} \sum_{\mathbf{R}_e} e^{i\mathbf{k}' \cdot \mathbf{R}_e} H_{\mathbf{0}, \mathbf{R}_e}^{el} \right) U_{\mathbf{k}'}^\dagger \quad (7)$$

$$D_{\mathbf{q}'}^{ph} = e_{\mathbf{q}'}^\dagger \left(\frac{1}{N_p} \sum_{\mathbf{R}_p} e^{i\mathbf{q}' \cdot \mathbf{R}_p} D_{\mathbf{0}, \mathbf{R}_p}^{ph} \right) e_{\mathbf{q}'} \quad (8)$$

$$g(\mathbf{k}', \mathbf{q}') = \frac{1}{N_e} \sum_{\mathbf{R}_e, \mathbf{R}_p} e^{i(\mathbf{k}' \cdot \mathbf{R}_e + \mathbf{q}' \cdot \mathbf{R}_p)} U_{\mathbf{k}'+\mathbf{q}'}^\dagger g(\mathbf{R}_e, \mathbf{R}_p) U_{\mathbf{k}'} e_{\mathbf{q}'} \quad (9)$$

where $N_e = N_1^k \times N_2^k \times N_3^k$ is the number of unit cells in real space.

Density functional theory (DFT) and density functional perturbation theory (DFPT) calculations were performed as implemented in the Quantum Espresso code. ^[38] Norm-conserving pseudopotential with the Perdew-Burke-Ernzerhof (PBE)^[52] exchange-correlation functional was used for the tin atom. For the structure optimization and the plane wave cutoff energy, convergence threshold for total energy and force were set to be 65 Ry, 10^{-12} Ry and 10^{-6} Ry/bohr, respectively. For the phonon dispersion calculations, a k-mesh of $20 \times 20 \times 1$ was used for the self-consistent DFT calculation, while the force

constants were obtained with a $5 \times 5 \times 1$ \mathbf{q} -mesh. The Wannier interpolation method was used to obtain ultra-dense electronic structure, phonon dispersion and el-ph couplings matrix as implemented in the Wannier90^[39] and EPW code.^[40,41] The el-ph coupling matrix was interpolated from $10 \times 10 \times 1$ coarse \mathbf{k} -mesh and $5 \times 5 \times 1$ coarse \mathbf{q} -mesh to $120 \times 120 \times 1$ k- and q-meshes for stanene. In graphene, the el-ph coupling matrix was interpolated from $6 \times 6 \times 1$ coarse \mathbf{k} -mesh and $6 \times 6 \times 1$ coarse \mathbf{q} -mesh to $120 \times 120 \times 1$ k- and q-meshes. Gaussian broadening of 0.045 eV were used for the delta-function in calculating the relaxation time in Equation (2) We excluded el-ph couplings for phonons with frequency lower than 5 cm^{-1} .

Deformation potential theory. The el-ph coupling can be given by

$$g_{\lambda q}(\mathbf{k}, n, n') = \sqrt{\frac{\hbar}{2M\omega_{\lambda q}}} M_{\lambda q} \quad (10)$$

where the coupling matrix

$$M_{\lambda q} = \left\langle \psi_{n\mathbf{k}} \left| \frac{\partial V_{scf}}{\partial u_{\lambda q}} \cdot \mathbf{e}_{\lambda q} \right| \psi_{n'\mathbf{k}+q} \right\rangle \quad (11)$$

The deformation potential approximation assumes that for long wavelength limit ($|\mathbf{q}| \sim 0$), the LA phonon is the dominant scattering process and the coupling matrix could be expressed in terms of the deformation potential constant D_{LA} ^[46]

$$M_{\lambda q} = D_{LA} |\mathbf{q}| \quad (12)$$

By assuming elastic scattering, the approximate relaxation time is given by

$$\frac{1}{\tau_{nk}} = \frac{2\pi k_B T D_{LA}^2}{\hbar C_{ii}} \sum_{n\mathbf{k}} \delta(\varepsilon_{n'\mathbf{k}'} - \varepsilon_{n\mathbf{k}}) (1 - \cos \theta_{\mathbf{k}, \mathbf{k}'}) \quad (13)$$

where elastic constant $C_{ii} = \rho \mathbf{v}^2$ where ρ is mass density and \mathbf{v} is the sound velocity corresponding the LA phonon. Since the wavelength of the latter is much larger than the lattice spacing, the deformation potential can be simulated by dilating the unit cell.

The elastic constant in Eq. (13) is calculated by fitting parabolic of the total unit cell energy shift $(E - E_0)$ with respect to the lattice strain $\Delta l/l_0$:

$$\frac{E - E_0}{S_0} = \frac{C_{ii}}{2} \left(\frac{\Delta l}{l_0} \right)^2 \quad (14)$$

where E_0 and S_0 are the equilibrium total energy and area of the unit cell for 2D materials.

The deformation potential constant D_{LA} is obtained by fitting linear of the Fermi energy shift $\Delta\epsilon_F$ with lattice strain $\Delta l/l_0$ the Dirac cone materials

$$\Delta\epsilon_F = D_{LA} \left(\frac{\Delta l}{l_0} \right) \quad (15)$$

Computational details can be found in supporting information.

Supporting Information

Comparison of the band structure and phonon dispersion calculated from both DFT and Wannier extrapolation scheme. Computational details of deformation potential theory. Mobility data obtained from DPA and full electron phonon couplings approaches. These are given in the Supporting Information, available from the Wiley Online Library or from the author.

Acknowledgements

ZS is deeply indebt to Prof. Daoben Zhu for his insightful discussions, continuous encouragements, and fruitful collaborations, which led to more than 30 co-authored publications in the past 15 years. In the occasion of the 75th anniversary, the authors would like to express their sincere wishes to Professor Daoben Zhu for good health and longevity. This work is supported by the National Natural Science Foundation of China (Grant nos. 21673123, 21290190, and 91333202) and the Ministry of Science and Technology of China (Grant nos. 2013CB933503 and 2015CB655002). Computational resources were provided by the Tsinghua University High Performance Supercomputing Center.

Received: ((will be filled in by the editorial staff))

Revised: ((will be filled in by the editorial staff))

Published online: ((will be filled in by the editorial staff))

References

[1] K. S. Novoselov, A. K. Geim, S. V Morozov, D. Jiang, Y. Zhang, S. V Dubonos, I. V Grigorieva, A. A. Firsov, *Science* **2004**, *306*, 666.

- [2] A. K. Geim, K. S. Novoselov, *Nat. Mater.* **2007**, *6*, 183.
- [3] K. S. Novoselov, A. K. Geim, S. V. Morozov, D. Jiang, M. I. Katsnelson, I. V. Grigorieva, S. V. Dubonos, A. A. Firsov, *Nature* **2005**, *438*, 197.
- [4] D. Li, R. B. Kaner, *Science* **2008**, *320*, 1170.
- [5] A. Gupta, T. Sakthivel, S. Seal, *Prog. Mater. Sci.* **2015**, *73*, 44.
- [6] P. Vogt, P. De Padova, C. Quaresima, J. Avila, E. Frantzeskakis, M. C. Asensio, A. Resta, B. Ealet, G. Le Lay, *Phys. Rev. Lett.* **2012**, *108*, 155501.
- [7] L. Li, S. Z. Lu, J. Pan, Z. Qin, Y. Q. Wang, Y. Wang, G. Y. Cao, S. Du, H. J. Gao, *Adv. Mater.* **2014**, *26*, 4820.
- [8] S. Balendhran, S. Walia, H. Nili, S. Sriram, M. Bhaskaran, *Small* **2015**, *11*, 640.
- [9] Y. Xu, B. Yan, H.-J. Zhang, J. Wang, G. Xu, P. Tang, W. Duan, S.-C. Zhang, *Phys. Rev. Lett.* **2013**, *111*, 136804.
- [10] L. Matthes, O. Pulci, F. Bechstedt, *J. Phys. Condens. Matter* **2013**, *25*, 395305.
- [11] F. Zhu, W. Chen, Y. Xu, C. Gao, D. Guan, C. Liu, D. Qian, S.-C. Zhang, J. Jia, *Nat. Mater.* **2015**, *14*, 1020.
- [12] C. L. Kane, E. J. Mele, *Phys. Rev. Lett.* **2005**, *95*, 226801.
- [13] X. L. Qi, S. C. Zhang, *Rev. Mod. Phys.* **2011**, *83*, 1057.
- [14] M. Z. Hasan, C. L. Kane, *Rev. Mod. Phys.* **2010**, *82*, 3045.
- [15] Y. Yao, F. Ye, X. L. Qi, S. C. Zhang, Z. Fang, *Phys. Rev. B* **2007**, *75*, 2.
- [16] Y. Xu, Z. Gan, S.-C. Zhang, *Phys. Rev. Lett.* **2014**, *112*, 226801.
- [17] B. Peng, H. Zhang, H. Shao, Y. Xu, X. Zhang, H. Zhu, *Sci. Rep.* **2016**, *6*, 20225.
- [18] R. Yu, W. Zhang, H.-J. Zhang, S.-C. Zhang, X. Dai, Z. Fang, *Science* **2010**, *329*, 61.
- [19] Y. Shaidu, O. Akin-Ojo, *Comput. Mater. Sci.* **2016**, *118*, 11.
- [20] M. Ezawa, *J. Phys. Soc. Japan* **2015**, *84*, 012001.
- [21] M. Long, L. Tang, D. Wang, L. Wang, Z. Shuai, *J. Am. Chem. Soc.* **2009**, *2*, 17728.
- [22] M. Long, L. Tang, D. Wang, Y. Li, Z. Shuai, *ACS Nano* **2011**, *5*, 2593.

[23] J. Bardeen, W. Shockley, *Phys. Rev.* **1950**, *80*, 72.

[24] J. Xi, M. Long, L. Tang, D. Wang, Z. Shuai, *Nanoscale* **2012**, *4*, 4348.

[25] J. Xi, D. Wang, Y. Yi, Z. Shuai, *J. Chem. Phys.* **2014**, *141*, 34704.

[26] K. M. Borysenko, J. T. Mullen, E. A. Barry, S. Paul, Y. G. Semenov, J. M. Zavada, M. B. Nardelli, K. W. Kim, *Phys. Rev. B* **2010**, *81*, 3.

[27] E. H. Hwang, S. Das Sarma, *Phys. Rev. B* **2008**, *77*, 115449.

[28] K. Kaasbjerg, K. S. Thygesen, K. W. Jacobsen, **2012**, *165440*, 7.

[29] B. Liao, J. Zhou, B. Qiu, M. S. Dresselhaus, G. Chen, *Phys. Rev. B* **2015**, *91*, 235419.

[30] X.-S. Ye, Z.-G. Shao, H. Zhao, L. Yang, C.-L. Wang, *RSC Adv.* **2014**, *4*, 21216.

[31] Y. Cai, G. Zhang, Y. W. Zhang, *J. Am. Chem. Soc.* **2014**, *136*, 6269.

[32] T. Zhao, W. Shi, J. Xi, D. Wang, Z. Shuai, *Sci. Rep.* **2016**, *7*, 19968.

[33] T. Gunst, T. Markussen, K. Stokbro, M. Brandbyge, *Phys. Rev. B* **2016**, *93*, 35414.

[34] M. V. Fischetti, W. G. Vandenberghe, *Phys. Rev. B* **2016**, *93*, 155413.

[35] W. G. Vandenberghe, M. V. Fischetti, *J. Appl. Phys.* **2014**, *116*, 173707.

[36] S. Baroni, S. De Gironcoli, A. D. Corso, S. Scuola, I. Superiore, I. Istituto, F. Materia, I.- Trieste, P. Giannozzi, *Rev. Mod. Phys.* **2001**, *73*, 515.

[37] N. Marzari, A. a. Mostofi, J. R. Yates, I. Souza, D. Vanderbilt, *Rev. Mod. Phys.* **2012**, *84*, 1419.

[38] P. Giannozzi, S. Baroni, N. Bonini, M. Calandra, R. Car, C. Cavazzoni, D. Ceresoli, G. L. Chiarotti, M. Cococcioni, I. Dabo, A. Dal Corso, S. de Gironcoli, S. Fabris, G. Fratesi, R. Gebauer, U. Gerstmann, C. Gougaussis, A. Kokalj, M. Lazzeri, L. Martin-Samos, N. Marzari, F. Mauri, R. Mazzarello, S. Paolini, A. Pasquarello, L. Paulatto, C. Sbraccia, S. Scandolo, G. Sclauzero, A. P. Seitsonen, A. Smogunov, P. Umari, R. M. Wentzcovitch, *J. physicsCondensed matter* **2009**, *21*, 395502.

[39] A. A. Mostofi, J. R. Yates, G. Pizzi, Y. S. Lee, I. Souza, D. Vanderbilt, N. Marzari, *Comput. Phys. Commun.* **2014**, *185*, 2309.

[40] J. Noffsinger, F. Giustino, B. D. Malone, C. H. Park, S. G. Louie, M. L. Cohen, *Comput. Phys. Commun.* **2010**, *181*, 2140.

[41] S. Poncé, E. R. Margine, C. Verdi, F. Giustino, *Comput. Phys. Commun.* **2016**, *209*, 116.

[42] S. Cahangirov, M. Topsakal, E. Aktürk, H. Şahin, S. Ciraci, *Phys. Rev. Lett.* **2009**, *102*, 236804.

[43] C. C. Liu, H. Jiang, Y. Yao, *Phys. Rev. B* **2011**, *84*, 195430.

[44] D. Jose, A. Datta, *J. Phys. Chem. C* **2012**, *116*, 24639.

[45] X. Li, J. T. Mullen, Z. Jin, K. M. Borysenko, M. Buongiorno Nardelli, K. W. Kim, *Phys. Rev. B* **2013**, *87*, 121412.

[46] K. Kaasbjerg, K. S. Thygesen, K. W. Jacobsen, *Phys. Rev. B* **2012**, *85*, 115317.

[47] E. Mariani, F. Von Oppen, *Phys. Rev. Lett.* **2008**, *76801*, 076801.

[48] H. Şahin, S. Cahangirov, M. Topsakal, E. Bekaroglu, E. Akturk, R. T. Senger, S. Ciraci, *Phys. Rev. B* **2009**, *80*, 155453.

[49] Y. Ding, Y. Wang, *J. Phys. Chem. C* **2013**, *117*, 18266.

[50] I. Souza, N. Marzari, D. Vanderbilt, *Phys. Rev. B* **2001**, *65*, 35109.

[51] F. Giustino, M. Cohen, S. Louie, *Phys. Rev. B* **2007**, *76*, 165108.

[52] J. P. Perdew, K. Burke, M. Ernzerhof, *Phys. Rev. Lett.* **1996**, *77*, 3865.

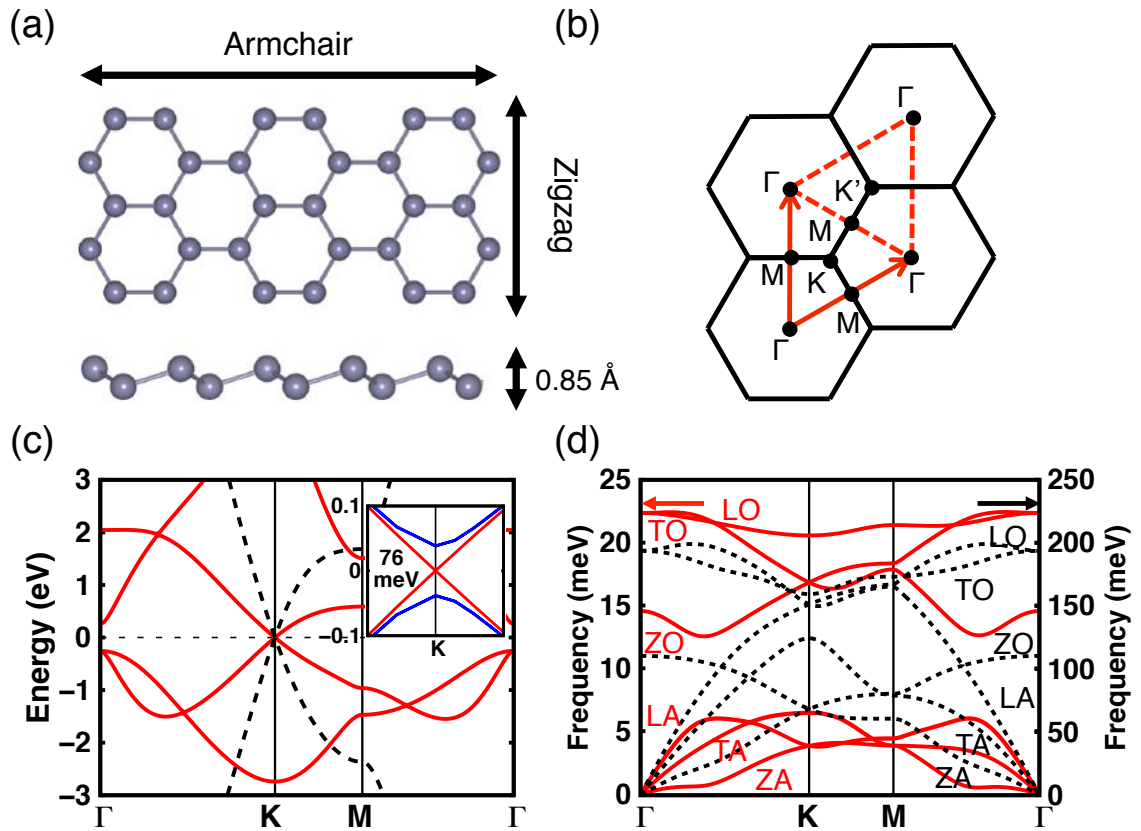


Figure 1. (a) Top and side view of stanene monolayer. (b) Schematic illustration of the first Brillouin zone and high symmetry points. (c) Band structures of graphene (black-dashed), stanene without SOC (red-solid) and with SOC (blue-solid, inset). (d) Phonon dispersions of graphene (black-dashed) and stanene (red-solid).

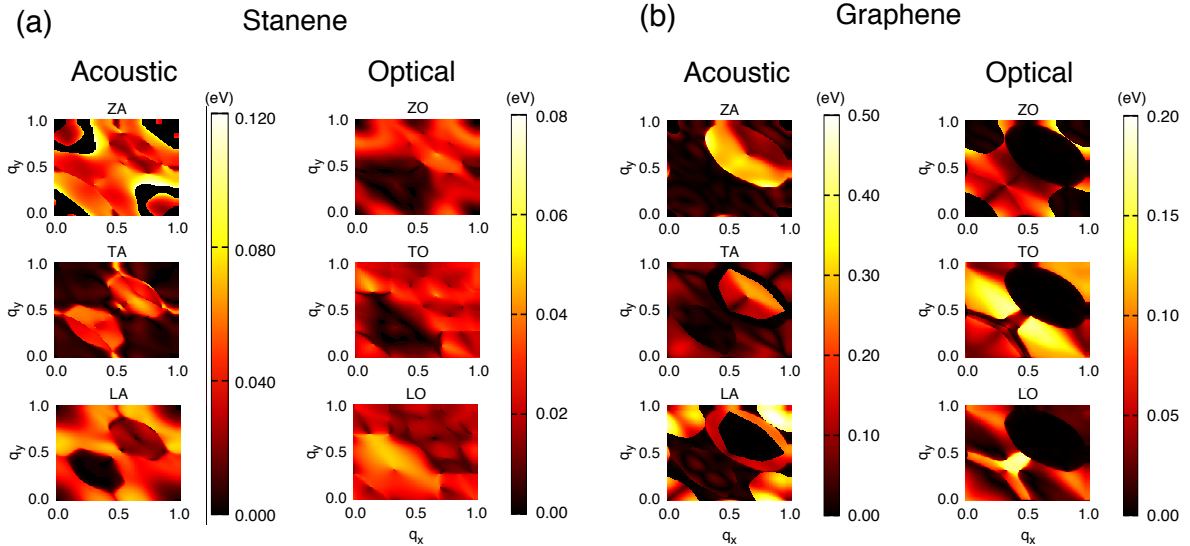


Figure 2. Electron-phonon coupling matrix of stanene (a) and graphene (b) as a function of q at a fixed k -point $K = (1/3, 1/3, 0)$ in the conduction band.

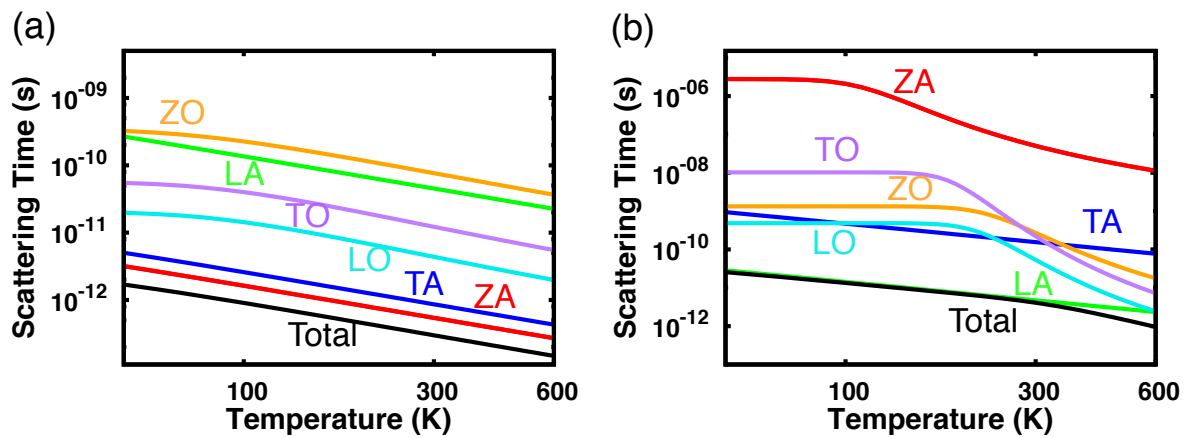


Figure 3. Temperature dependence of scattering time for the conduction band of stanene (a) and graphene (b) for all phonon modes. For graphene, the main contribution to scattering time is the LA phonon. Whereas for stanene, the ZA and TA phonon mode scattering and LA contribute the least.

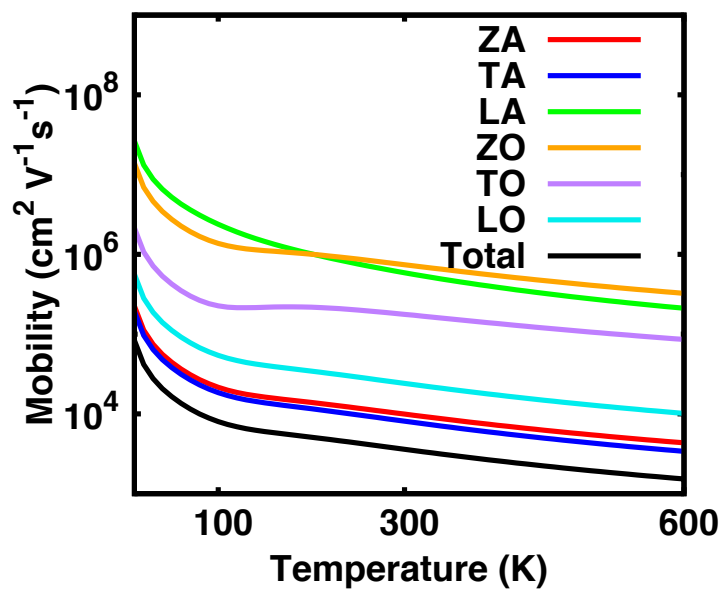


Figure 4. Temperature dependence of mobility for the conduction band of stanene with all phonon modes.

Table 1. Lattice constant, deformation potential constant D_{LA} , elastic constant C_{2d} and electron/hole mobility μ for stanene and graphene along a/b-direction at 300K. DP constants from full evaluation of el-ph coupling are given in parentheses

System	Buckling (Å)	Direction	Lattice Const. (Å)	D_{LA} (eV)	C_{2d} (J/m)	μ_e [$10^5 \text{cm}^2/(\text{V s})$]	μ_h [$10^5 \text{cm}^2/(\text{V s})$]
Stanene	0.85	zigzag	4.67	0.47 (0.52)	28.5	27.7	40.1
		armchair	8.09	0.48 (0.52)	28.6	24.4	35.2
Graphene	0.00	zigzag	4.27	5.00 (4.22)	328	3.32	2.05
		armchair	2.47	5.14(4.22)	328	3.32	2.05

Table. 2 Scattering rate of each phonon mode for graphene and stanene at Dirac point $\mathbf{K}=(1/3, 1/3, 0)$ and $T=300$.

Scattering Rate $1/\tau$ (1/s)	Stanene		Graphene	
	Hole	Electron	Hole	Electron
ZA	1.8×10^{12}	1.8×10^{12}	3.6×10^7	2.3×10^7
TA	1.2×10^{12}	1.2×10^{12}	2.6×10^{10}	6.4×10^9
LA	2.3×10^{10}	2.2×10^{10}	2.7×10^{11}	2.1×10^{11}
ZO	1.3×10^{10}	1.3×10^{10}	9.8×10^9	8.9×10^9
TO	8.2×10^{10}	8.2×10^{10}	1.4×10^{10}	1.4×10^{10}
LO	2.4×10^{11}	2.3×10^{11}	4.0×10^{10}	5.3×10^{10}
Total	3.4×10^{12}	3.4×10^{12}	3.6×10^{11}	3.0×10^{11}

Table 3. Intervalley scattering and intravalley scattering in the conduction bands for stanene and graphene at T =300 K.

Scattering Rate (1/s)	Stanene			Graphene		
	Intravalley	Intervalley	Total	Intravalley	Intervalley	Total
ZA	1.27×10^3	1.84×10^{12}	1.84×10^{12}	1.15×10^{-4}	2.33×10^7	2.33×10^7
TA	9.17×10^7	1.16×10^{12}	1.16×10^{12}	6.43×10^9	1.08×10^7	6.44×10^9
LA	1.74×10^{10}	4.68×10^9	2.21×10^{10}	2.12×10^{11}	5.89×10^7	2.12×10^{11}
ZO	2.01×10^8	1.29×10^{10}	1.31×10^{10}	1.41×10^7	8.83×10^9	8.85×10^9
TO	6.96×10^{10}	1.23×10^{10}	8.19×10^{10}	7.70×10^9	6.62×10^9	1.43×10^{10}
LO	6.62×10^{10}	1.62×10^{11}	2.29×10^{11}	5.66×10^9	4.75×10^{10}	5.32×10^{10}

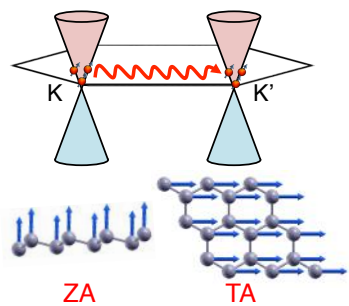
Table of contents

Roles of electron-phonon couplings are evaluated in stanene, the intrinsic electron and hole mobilities of $2\sim3\times10^3$ $\text{cm}^2 \text{ V}^{-1} \text{ s}^{-1}$ at 300K are found to be dominated by intervalley scatterings from the out-of-plane (ZA) and transverse acoustical (TA) modes of vibrations.

Keywords: stanene, electron-phonon couplings, carrier mobility calculation, density functional perturbation theory, two-dimensional materials

Yuma Nakamura¹, Tianqi Zhao¹, Jinyang Xi, Wen Shi, Dong Wang*, and Zhigang Shuai*

Intrinsic Charge Transport in Stanene: Roles of Electron-Phonon Couplings



Supporting Information

1. Band structure and phonon dispersion of stanene

To validate the Wannier extrapolation approach, we present in Figure S1 the band structure and phonon dispersion obtained from both original DFT calculation and that with Wannier extrapolation. It is seen they are identical, validating the method. The computational costs of the latter is much less than the former. And in the case of evaluating electron-phonon coupling, it is practically impossible for the former case.

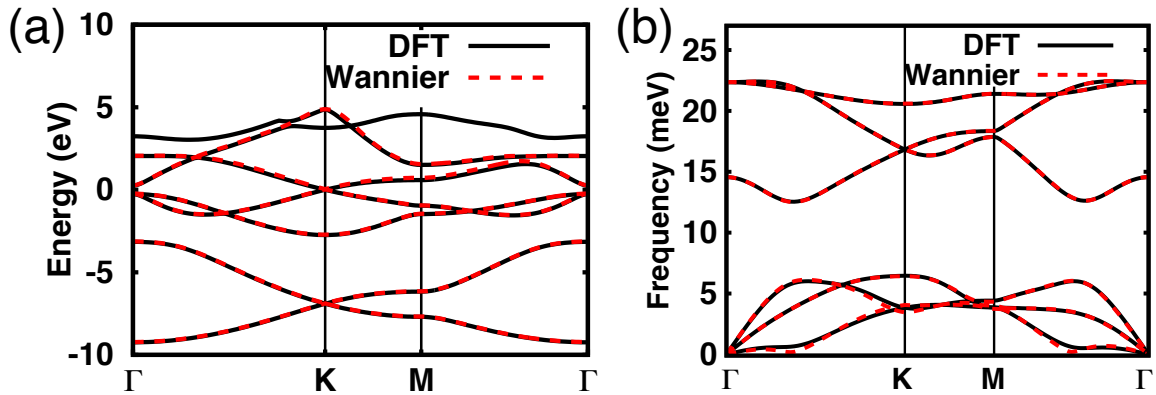


Figure S1. The Wannier interpolation (black solid) and DFT (red dashed) calculation of electronic structure (a) and phonon dispersion (b).

2. Computational details of deformation potential theory

The calculation under deformation potential approximation was based on the electric band structure using DFT with the projector augmented wave (PAW) method and Perdew-Burke-Ernzerhof (PBE) exchange and correlation functionals as implemented in the Vienna ab-initio simulation package (VASP). For stanene and graphene, the Monkhorst-Pack k -mesh of $11 \times 11 \times 1$ was used for charge density calculation. The cutoff energy for self-consistent calculation was set to 800 eV. Vacuum height was set to 20 Å to avoid the interaction with neighboring layers.

We dilated the supercell with lattice strain $\Delta l / l_0$ as a lattice deformation from -1.5% to 1.5%. The dilation is simulated in two directions, which are zigzag direction and armchair direction. The elastic constant is calculated by parabolic fitting of total energy as $(E - E_0) / S_0 = C_{ii} (\Delta l / l_0)^2 / 2$, where S_0 and E_0 are the equilibrium area and total energy of the unit cell of stanene. The deformation potential is obtained from linear fitting of Fermi energy shift according to $D_{LA} = \Delta \epsilon_{Fermi} / (\Delta l / l_0)$. **Figure S2** shows the fitting of elastic constant and deformation potential constant of stanene.

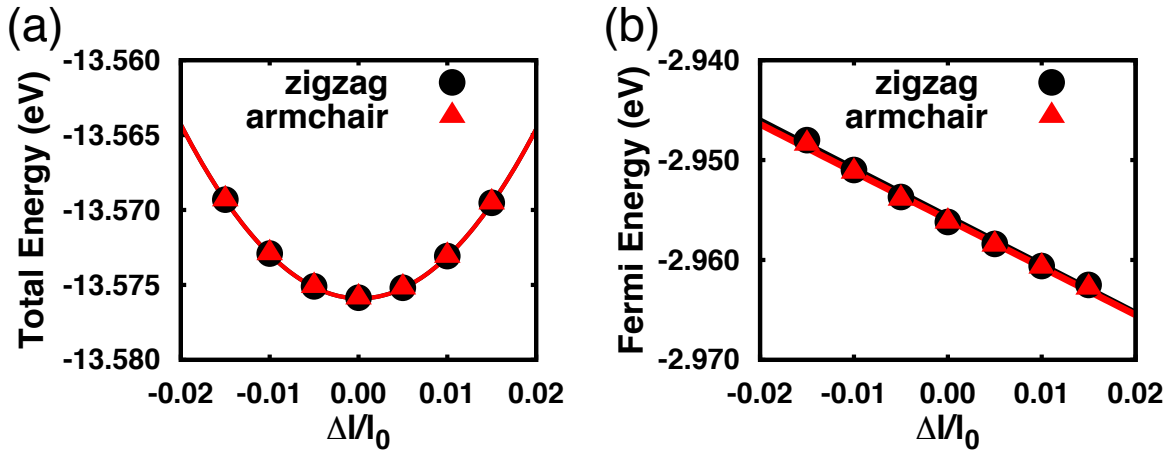


Figure S2. The total energy shift (a) and the Fermi energy shift (b) versus lattice dilation in stanene.

Table S1 Mobility for graphene and stanene calculated from deformation potential theory (DPA) and el-ph coupling matrix (EPC) at 300K. The bottom row is LA-limited mobility μ_{LA}^{EPC} . As expected from DPA, μ_{LA}^{EPC} of stanene is larger than that of graphene.

Mobility ($10^5 \text{ cm}^2 \text{ V}^{-1} \text{ s}^{-1}$)	Direction	Stanene		Graphene	
		Hole	Electron	Hole	Electron
μ^{DPA}	armchair	34.0	23.5	2.05	3.32
	zigzag	29.8	20.6	2.05	3.32
μ^{EPC}	armchair	0.0247	0.0250	1.97	2.56
	zigzag	0.0226	0.0281	2.02	2.61
μ_{ZA}^{EPC}	armchair	0.0483	0.0490	1.05×10^5	1.11×10^5
	zigzag	0.0428	0.0432	5.72×10^4	5.92×10^4
μ_{TA}^{EPC}	armchair	0.0727	0.0739	44.20	64.38
	zigzag	0.0684	0.0691	44.33	66.20
μ_{LA}^{EPC}	armchair	2.27	2.33	3.57	5.81
	zigzag	2.01	2.04	3.68	5.91